ing and W.

eider, D.H.,

98).
Phys. Rev.

Chapter 18

INTERACTIONS OF HIGHLY CHARGED IONS WITH FULLERENES

Uwe Thumm
J. R. Macdonald Laboratory, Department of Physics, Kansas State University
Manhattan, Kansas 66506--2604, USA

Abstract. When slow highly charged ions collide with complex targets, such as large atoms, clusters, and surfaces, they may capture many electrons into highly excited states, thereby leading to the temporary formation of unstable, multiply excited projectiles, commonly referred to as 'hollow ions'. Recent collision experiments with fullerene targets have made it possible to distinguish between hard collisions, which strongly favor fragmentation of the fullerene, and soft collisions, which primarily (multiply) ionize the fullerene. This chapter focuses on soft collisions of slow highly charged ions with gaseous C_{60} targets. It reviews models for multiple electron transfer and emission in comparison with a variety of recent measurements of electron capture cross sections, charge–state distributions, projectile deflection angles, and projectile kinetic energy gains. This comparison makes static and dynamic properties of fullerenes, such as ionization potentials and polarizabilities, observable in scattering experiments with charge–state and energy–selected beams of highly charged ions.

I. INTRODUCTION

The subject of this chapter lies intermediate between an ion-atom collision and an ion-surface collision. Collisions of highly charged ions (HCI) with many-electron atomic targets [1–5] and metal surfaces [6–21] have been a subject of intense experimental and theoretical interest for more than a decade, and several characteristics of the electron exchange and emission processes are becoming well established. More recently, insulator surfaces have been added to the list of target materials, and interesting new phenomena are being investigated [22–27]. For collisions with surfaces, recent experiments have measured the final charge state distribution of the surface–scattered projectile [7,14,19], the projectile deflection angle [22,28], and the emission of electrons [13,15,18,20,23,29] and photons [6,11,12,26] during and after the projectile–surface interaction.

The interaction of HCIs with insulating surfaces differs from their interaction with metal surfaces. One obvious difference is due to the very different conductivity that leads to the local accumulation of charges on insulators. In multi–capture events, capture–induced localized charges on the insulator

surface may influence the subsequent charge–transfer dynamics and the projectile trajectory. For metal targets these charges are instantaneously neutralized and irrelevant on the time scale that governs electronic ion–target interactions. Another important difference is given by the electronic band structure of the target surface. An approaching highly charged projectile first captures electrons from the highest occupied target levels, such that the location of the Fermi level, i.e. the work function of the target, becomes an important substrate–dependent parameter in the description of the charge exchange process. As a consequence, the critical ion–surface distance where electron capture begins can be approximated by a simple analytical expression as a function of the target ionization potential and the charge state of the incident projectile [9]. Differences in the charge transfer dynamics also arise due to the availability of unoccupied surface states above the Fermi level, which may allow for the recapture (resonant loss) of a previously captured electron that is energetically shifted across the Fermi level and into resonance with the unoccupied part of the conduction band as the projectile approaches a metal surface. For typical insulator targets, this resonant loss channel is closed since a broad band gap is located above the Fermi level.

For the case of a metal surface, the classical over-barrier transfer of loosely bound delocalized electrons resembles field ionization and begins at a projectile-surface distance for which the reduction of the potential barrier allows for the departure of electrons at the top of the Fermi sea. Since a surface offers an infinite reservoir of electrons with binding energies equal to the work function of the material, the interaction with an HCI is usually accompanied by multiple electron transfer, i.e. with a flow of electrons towards the projectile. Similarly, for atomic targets the transfer of successively more tightly bound electrons to the HCI occurs at successively smaller impact parameters. As for target surfaces, the simplest physical description attributes the capture to an over-barrier transfer of target electrons to the projectile. So called 'Classical Over-barrier Models (COM)' that are based on this picture have been remarkably successful [9,24,30–32,48,51]. As for the case of an insulating target surface, gaseous atomic targets carry capture–induced positive charges that influence subsequent capture processes.

Cluster targets, in particular C_{60}, combine several of the features of charge transfer from atoms in the gas phase and from surfaces. A sketch of the collision scenario including the formation of hollow ions due to resonant electron capture and their downstream decay is shown in Figure 1. Relevant time scales for a typical collision system are in the femto second range and are assembled in Table I. Similar to a solid surface, C_{60} provides a large reservoir of electrons with nearly the same binding energies and thus the cross section for the transfer of many electrons falls slowly with the number of electrons captured. As for an insulating target surface or an atomic target, electron capture by an HCI results in a multiply charged target. Large metallic clusters and C_{60} have band structures similar to metal surfaces with regard to a large portion of unoccupied states above the Fermi level. Smaller clusters tend to form narrowly spaced levels, rather than bands and, with regard to capture, may resemble a large atomic target. Furthermore, as in soft ion-atom interactions, the geometry of ion–cluster collisions may allow slow projectiles to avoid the nearly complete neutralization which accompanies reflection from a surface [7]. This difference between cluster and surface targets is enhanced by the image charge acceleration [28] which poses an upper limit for the closest approach of the ion to the surface and complicates the distinction between above, near, and below surface interactions [15,20].

In contrast to HCI–surface collisions, for cluster targets the 'hollow atom' formed in the sequence of capture processes is not necessarily destroyed in the encounter, but is likely to survive and deexcite far downstream. This offers the possibility of examining the complicated relaxation dynamics of multiply excited ions on the exit trajectory and at large distances where electron capture has ceased. Collisions with clusters are also similar to the ion-atom case in that an intact recoil ion often remains whose charge state can be used to determine the number of electrons initially removed from the

target. In recent years, several groups have been exploiting these characteristics of the ion-cluster collisions for the special case of collisions with neutral C_{60} in order to establish connections between our more mature understanding of ion-atom and ion-surface collisions [16,33–53]

The growing popularity of C_{60} in collision experiments is linked to the convenience with which it is handled in the laboratory and to the availability of pure C_{60} in macroscopic amounts. In contrast to metal clusters, a target of specific mass is ready to be used. The truncated icosahedral molecular structure of C_{60} and its large number of vibrational degrees of freedom make the highly symmetrical cluster with 240 valence electrons unusually stable [53]. Due to its relatively large thermal stability, C_{60} can be evaporized easily and serve as a gaseous target for incoming electrons [54,55], ions [47,53], and charged clusters [56]. The cage-structure of C_{60} was observed to withstand the reflection from a surface [57], and photoionization and collision experiments with highly charged ions (HCI) have produced C_{60}^{i+} ions in positive charge states up to i=9 [38] that do not dissociate for at least several micro seconds.

With respect to the projectile, high charge states of the incoming ions are particularly suitable for investigations of the dynamic electronic response of C_{60} clusters to a strong external perturbation that may significantly distort the electronic charge distribution of the easily polarizable target and lead to the capture and emission of a relatively large number of electrons. The analyses and theoretical modeling of such collisions constitute not only an important tool for examining the static and dynamic properties of fullerenes and their basic interaction mechanisms with highly charged projectile ions, but also allow for the study of the complicated electronic dynamics involved in the collisional creation and post-collisional decay of unstable and multiply excited projectiles due to Auger electron and X-ray emission [37,38,45,51]. For example, in recent coincidence experiments the deflection of slow Ar^{8+} projectiles was found to depend sensitively on the dynamic polarizability of the target [35].

A significant amount of work in the emerging field of slow HCI–C_{60} interaction studies was stimulated by experiments done at Kansas State University and the University of Giessen by Walch *et al.* [34]. These experiments first probed the interaction between slow, HCIs and gaseous C_{60} targets by measuring the final charge–states of target and projectile in coincidence. The coincidence measurement allowed for the distinction between hard collisions at relatively small impact parameters which lead to fragmentation of the target–carbon cage, and non–destructive, soft collisions. Soft collisions occur at relatively large impact parameters, result in the capture of a relatively small number of electrons, and do not lead to the immediate fragmentation of the target. To some extent, in such distant collisions, fullerenes may be viewed as spherically shaped mono layers of graphite surfaces. As this distant view suggests, soft HCI—C_{60} collisions may allow for the undistorted investigation of 'above surface' effects, which are disguised by the image-charge attraction in grazing surface collisions [20]. Very recently, triple coincidence measurements have been performed [45] in which the ejected number of electrons is detected together with the final charge state of the projectile and the mass and charge of the recoiling target (or fragment).

This chapter will focus on resonant electron exchange and the emission of projectile Auger electrons during and after soft collisions of an HCI with C_{60}. Section II will give a brief overview of the dynamical COM. Numerical examples for charge–state evolutions and emitted electron yields follow in Section III. In the subsequent sections, the COM predictions for the following observables are discussed and compared with recent experiments: cross sections for the capture of a specific number of target electrons (Section IV), final projectile charge states (Section V), the projectile kinetic image energy gain (Section VI), and the projectile scattering angle (Section VII). With respect to the downstream relaxation of hollow ions (Section V), we propose a simple relaxation

scheme that includes auto–ionizing and radiative transitions. As a consequence of this downstream relaxation, almost all of the resonantly captured electrons are emitted. Section VIII includes remarks on some open questions regarding the localization and mobility of capture–induced charges on C_{60}. Conclusions follow in Section IX. Unless otherwise stated, atomic units are used throughout this chapter.

II. MODELS FOR THE FORMATION OF HOLLOW IONS

The main aspects of the interaction between slow highly charged ions and complex atomic or molecular targets can be described by using mostly classical model assumptions. In COMs the electronic interaction with highly charged ions is modeled within the independent electron picture and is based on the effective potential to which an active electron, i.e. an electron that might be captured or lost, is subjected. An important feature of this effective potential is the potential barrier located between target and projectile. Position and height of the barrier change during the collision due to the relative motion and changing electronic structure of the collision partners. The COM allows for resonant transitions if the motion of a target or projectile electron across the potential barrier is classically possible, if the initial electronic state is at least partly occupied, and if the final state is not fully occupied in order to prevent Pauli blocking. In the past, various versions of over–barrier models have been successfully applied to slow collisions of ions with atoms [30–32], surfaces [9,27], and clusters [16,34,35,48,49,51]. The model of Bárány and Setterlind [16] represents C_{60} as a dielectric sphere. Radius a and dielectric constant ϵ of the sphere are free parameters. For limiting values of these parameters particular types of targets are recovered within this approach: $\epsilon \to \infty$ models a perfectly conducting target, small values for a represent atomic or cluster targets, and $a \to \infty$ corresponds to scattering off a surface. For application to collisions of slow Ar^{8+} with C_{60} this model agrees well the experiment and other theories [34,48].

The common attractive feature in all COMs is, that basic ideas of classical dynamics and electrostatics yield reasonable estimates for charge–transfer cross sections, charge–state distributions, and other observables, that are beyond the technical feasibility of full quantum calculations. Details of the best specific formulation of the model remain under investigation. For very slow projectiles, ionization of the target occurs slowly with a minimum of transfer of electronic energy, leaving the C_{60} vibrationally and electronically cold, with a high probability of surviving the ionization intact. In the experiment of Walch et al. [34] it was shown that C_{60}^{i+} up to i=6 could be produced in this manner for slow Ar^{8+} ions on C_{60}, with relevant impact parameters in the range of typically 10 to 30 a.u.. Jin et al. [38] used a more highly charged projectile, Bi^{44+}, to produce C_{60}^{9+}, the most highly charged free C_{60}^{i+} ion reported to date. For charge states i<9, Jin et al. found C_{60}^{i+} ions to have lifetimes of at least 5μsec.

During the ion–cluster interaction, energy levels, level occupations, transition rates, and total charges of target and projectile vary as a function of R, the distance between the centers–of–mass of target and projectile. For the slow collisions considered in this chapter, R does not change on the time scale of resonant electronic transitions, and an adiabatic approximation is generally justified. In order to be captured or recaptured, the active electron is required to overcome the potential barrier V_B between target and projectile that is formed by the total electronic potential

$$V(q_p, q_t, R, z) = -\frac{q_p}{|R-z|} - \frac{q_t}{z} + V_{im}(q_p, R, z) \qquad (1)$$

where q_p and q_t are the charges of projectile and target acting on the electron in transition. The electron coordinate along the 'inter-nuclear axis' is denoted by z. The image potential V_{im} includes the active electron's interaction with its own image charge and with the image of the effective projectile charge q_p in the target. The barrier height V_B is found numerically for any distance R as the maximum of $V(q_p, q_t, R, z)$, considered as a function of z.

As the projectile approaches the target, the first resonant transfer of an electron becomes possible at the distance R_1^* between the projectile and target centers–of–mass, when V_B energetically moves below the highest occupied target level. Similarly, as R decreases, a second, third, etc. electron may be captured at critical distances $R_2^* > R_3^* \ldots$ on the incoming trajectory. Note that for the purpose of investigating electron capture mechanisms, the heavy projectile may be assumed to move along a straight–line trajectory (see Section VII for the experimental and computational verification of very small scattering angles of the order of a few mrad). The critical distances R_i^* are then equal to critical impact parameters at which the trajectory becomes tangent to a sphere of radius R_i^* about the target center. Since the *dynamical* COM discussed in this chapter treats the electronic charge as a continuous parameter, some assumption has to be made as to when a complete elementary charge has been transferred. This leaves some freedom in the precise definition of critical radii. In this chapter R_1^* is defined as the impact parameter at which charge begins to flow from the target to the projectile, and R_2^* as the impact parameter at which one unit of charge has left the target, etc.

The projectile may be described within an independent electron approach, based on hydrogenic shells n with energy levels, occupation numbers, and degeneracies denoted by $\epsilon_n^p(R)$, $a_n(R)$, and $A_n = 2n^2$, respectively. During the collision, projectile energy levels shift due to image–charge effects, Stark shifts induced by a charged target, and the dynamical change in screening induced by varying level populations. Target energy levels $\epsilon_m^t(R)$ are shifted downward in the strong attractive electric field of the positive projectile. After the capture of target electrons, positive charge accumulates on the target, which results in an additional downward shift of the target and projectile spectra (cf. Fig. 2 below).

The time evolution of the occupations $a_n(t)$ and $b_m(t)$ of projectile shells n and target levels m are obtained by integrating classical rate equations of the form

$$\frac{d}{dt}a_n = \Gamma_{RN} - \Gamma_{RL}\, a_n + \sum_{n'>n} \Gamma_{n',n} - 2\sum_{n'<n} \Gamma_{n,n'} \tag{2}$$

$$\frac{d}{dt}b_m = \Gamma_{RL}\, a_n - \Gamma_{RN}, \tag{3}$$

together with the known initial occupations of projectile and target, a_n^0 and b_m^0. Analytical expressions for the resonant–capture rates Γ_{RN} and resonant–loss rates Γ_{RL} can be derived as classical transfer currents [48,50]. Resonant transition rates and occupation numbers depend on $R(t)$, and the above equations are solved simultaneously with Newton's equation for the projectile motion. Since all rates depend on the level occupations a_n or b_m, equations (2) and (3) together with the equation of motion for the projectile constitute a non–linear set of coupled differential equations that needs to solved numerically. In particular, the resonant neutralization rate Γ_{RN} depends on the populations b_m of all (shifted) target levels m that lie within a small interval around the (shifted) energy of the resonant projectile level n. I note in passing that within the dynamical COM this 'energy binning' is necessary in order to relate classical transfer currents to discrete quantum levels [48,50]. For the two last terms in equation (2) it is sufficient to only include fast Auger transitions for which the two

active electrons start in the same shell and which may, to a small extent, deexcite a multiply excited projectile while competing resonant electron transfer occurs. Analytical approximations to these fast Auger rates were obtained by Burgdörfer *et al.* [8] by fitting atomic structure calculations. The Auger transition rates Γ_{n_1,n_2} include statistical weights to take into account the number of electrons in the initial and final active shells. Slow Auger relaxation channels are not included in equation (2) as they can be neglected *during* the collision (cf. Table I). Further downstream, however, when resonant transfer processes are classically forbidden, slow Auger processes become crucial in determining the final charge–state of the projectile. Downstream Auger and radiative relaxation steps determine the observable final charge state of the projectile and can be accounted for by enhancing the dynamical COM with a relaxation scheme [51] (see Section V below).

In order to understand how the occupation of target and projectile levels changes in response to resonant electron transfer processes, it is instructive to look at the energies of strongly coupled target and projectile levels relative to the top of the potential barrier as a function of $R_\parallel$, the projection of the distance between the target center–of–mass and the projectile onto the incident beam direction (cf. Fig. 1). For 80 keV (corresponding to a speed v=0.28) Ar^{8+} ions colliding with C_{60} with impact parameter $b = 15$, Figure 2 shows that projectile level $n = 6$ crosses the highest occupied target level (the Fermi level), labeled '$m = 15$'. The crossing happens above the potential barrier and near the point of closest approach. This results in a large current of target electrons from level $m = 15$ that are classically allowed to transfer to projectile level $n = 6$. Similarly, projectile level $n = 7$ crosses the same target level on the incident trajectory and above the barrier. The rapid resonant filling of projectile levels $n = 6$ and 7 is seen in Figure 3a (see Section III). In the calculation underlying Figure 2, the asymptotic target levels were taken from the local density functional (LDA) calculation of Puska and Nieminen [58]. In this calculation, the occupied valence states of C_{60} are represented by 15 highly degenerate levels.

The ground–state electronic structure of neutral C_{60} is well understood from first–principles calculations [50,59–61]. In the applications to charge exchange and electron emission in soft ion–C_{60} collisions discussed below, multi–center self–consistent Dirac–Fock–Slater (DFS) calculations [50,61] were employed to obtain ground–state electronic structures of neutral C_{60} and its positive ions $C_{60}^{i+}, i = 0...6$. In these calculations it was assumed that the cage structure does not change with the charge state i, matching the Buckyball radius $a = 6.7$ [59,58]. The calculations yield DFS single particle energies of C_{60}^{i+} for $i = 0 \ldots 7$ and the sequence of ionization potentials $I_{i=1...7} = 7.24, 10.63, 14.01, 17.44, 20.78, 24.24$, and $27.54\ eV$, in good agreement with other calculated [50,58–61] and experimental data [54,62,63]. Higher ionization potentials I_i, $i > 7$ can be approximated by taking into account the work necessary to remove an eighth, etc., electron from the surface of a conducting sphere, $I_i = I_1 + (i-1)/a$ [48]. In agreement with the simple electrostatical picture that represents the charged C_{60} cluster as a uniformly charged sphere, the incremental increase of ionization energies is only due to the net charge of the cluster, and the sequence of ionization energies increases linearly with the net cluster charge.

In comparison with the LDA calculation of Puska and Nieminen [58], the DFS calculation shows noticeable differences in the calculated valence spectra of neutral C_{60}. However, the comparison of scattering calculations based on the two different descriptions of the target–electronic structure [50] shows that cross sections for the production of specific target–charge states in soft collisions, charge state evolutions of target and projectile, and projectile scattering angles agree within 10 per cent.

An alternative interesting effort to calculate angle–differential scattering cross sections in HCI–C_{60} collisions has been made by Sakurai and Bárány [64]. This approach uses approximated Landau–Zener transition rates and classical potential scattering theory.

III. CHARGE–STATE EVOLUTION AND ELECTRON EMISSION

Typical charge–state evolutions in HCI–C_{60} interactions are given in Figure 3, where changes in occupation numbers (i.e. the instantaneous occupation minus the initial occupation of a particular projectile level) are shown as a function of $R_\parallel$. The figure shows results for incident Ar^{8+} at a kinetic energy of 80 keV on a trajectory with impact parameter $b = 15$ (Fig. 3a) and Bi^{46+} at 800 keV with $b = 25$ (Fig. 3b). For the Ar^{8+} projectile, the $n = 6$ and 7 shells get resonantly populated on the incoming trajectory (cf. Fig. 2), in agreement with experimental evidence for capture into the $n = 7$ shell [34,39]. Auger relaxation of the projectile on the outgoing trajectory ($R_\parallel > 0$) leads to the partial depletion of projectile shells $n = 6$ and 7 and increases the population in projectile levels with $n = 3$ and 4.

An extreme population inversion is achieved with incident Bi^{46+} projectiles. Figure 3b shows that resonant transitions first populate projectile shell $n = 31$ and, as the projectile further approaches the target, eventually lead to the population of shells with principal quantum numbers between 19 and 31. With respect to the target, the dynamical COM predicts a large current of resonantly captured electrons that originate in energetically densely spaced, occupied levels near the Fermi level of C_{60} [51]. In general, the large flux of captured electrons is accompanied by a very small flux of previously captured electrons that are lost to initially unoccupied target levels above the Fermi level. The projectile continues to relax by emitting electrons as it moves further away from the target and after charge exchange has become impossible (see Section V below). The charge–state evolutions in Figure 4 follow directly from the time–dependent occupations in equations (2) and (3). Auger transitions are too slow to significantly depopulate excited projectile levels within the short collision time interval of about 15 fs covered in Figures 3a and 4. The displayed accumulated current of emitted Auger electrons in Figure 4 and the increase of the net projectile charge on the displayed part of the outgoing trajectory are therefore very small.

The charge states of target and projectile as a function of the impact parameter and at a distance $R_\parallel = 150$ on the outgoing trajectory are shown in Figure 5. At this distance all resonant electron transfer has stopped. The comparatively slow projectile Auger transitions had no time to relax the projectile. A lower limit for the impact–parameter range of non–destructive collisions is given by the highest charge state the target ions support without falling apart while interacting with the projectile. At the smallest impact parameter $b = 15$ in Figure 5a, the incident Ar^{8+} ion captures five electrons and thus maintains the carbon cage of the target [34]. At the smallest impact parameter in Figure 5b, the incident Bi^{46+} has captured a large number of electrons, eventually leading to fragmentation of the target. In this case, the dynamical COM is applicable under the realistic assumption that the multiply charged fullerene is stable *during* the collision, i.e. at least for several femto seconds.

IV. CROSS SECTIONS FOR MULTIPLE ELECTRON CAPTURE

As Figures 3 and 4 illustrate, an HCI captures severals electrons on the incident trajectory. The sequence of critical radii R_i^* for the capture of i electrons can be extracted from the impact parameter dependence of the final target charge state shown in Figure 5. Values for 50 keV N^{5+} [49], $3.3q$ keV Ar^{q+}, $q = 8, 15$ [52], and 830 keV Bi^{46+} [51] colliding with C_{60} are given in Table II. The

critical distances R_i^* for sequential over–barrier capture are related to geometrical cross sections for the production of specific charge states, $+i$, of C_{60} by

$$\sigma_i = \pi({R_i^*}^2 - {R_{i+1}^*}^2) \tag{4}$$

and to the total geometrical cross section for charge exchange in non–destructive collisions by $\sigma_{tot} = \pi {R_1^*}^2$.

The calculated COM total cross sections agree with the absolute measurements for incident Argon ions performed by Walch *et al.* [34,48] and by Selberg *et al.* [39,52]. The cross sections in Table III are based on the critical radii in Table II. As expected, the simulated cross sections for incident 50 keV N^{5+} ions [49] are smaller than for slow Ar^{8+} projectiles. For N^{5+} resonant over–barrier capture of delocalized electrons in distant collisions does not lead to fragmentation of C_{60}, in contrast to experimental [34] evidence for 80 keV Ar^{8+} impact . Thus capture–induced fragmentation appears to require a minimal interaction strength that is not reached for N^{5+} ions at 50 keV impact energy.

V. DOWNSTREAM RELAXATION OF HOLLOW IONS

Hollow ions, that were created in ion–cluster collisions, decay during the typically several micro seconds of flight time needed by the projectile to cover the macroscopic distance between the collision (resonant–exchange) region and the detector (cf. Fig. 1 and Table I). This downstream decay can be modeled as a sequence of auto–ionizing and radiative relaxation steps [51]. Typically the HCI starts to relax via a cascade of Auger transitions. During these transitions lower lying levels are populated. Later, when the Auger relaxation cascade has populated lower–lying shells, radiative transitions may start to compete for subsequent relaxation steps. This is in agreement with typical branching ratios (radiative versus non–radiative transitions rates) which put increasing weight on radiative transitions as lower shells get populated. Radiative relaxation steps may then proceed along the 'Yrast' line of maximal angular momentum of the active electron. This is supported by the statistical dominance of high angular momentum states, the dipole selection rule ($\Delta l = 1$), and the resonant population of high angular momentum states at large impact parameters.

Several attempts to model the intricate relaxation of multiply excited ions have been made in the past. Benoit–Cattin et al. [4] have investigated the relaxation of doubly, triply, and quadruply excited projectile states formed in collisions of 70 keV N^{7+} ions with Argon. Their discussion of possible relaxation paths is based on measured electron spectra in conjunction with predictions of the classical over–barrier model of Niehaus [31] for the formation of the hollow ion. The emitted electron spectra are dominated by doubly excited lines which are traced to excited states formed by either direct double capture or auto–ionizing cascades. Radiative stabilization following double electron capture of 10 keV/amu Ar^{q+}, $q \leq 17$ and Kr^{q+}, $q \leq 34$ ions colliding with Argon has been discussed by Ali et al. [5]. Radiative stabilization was found to be of importance for the case of 'asymmetric' doubly excited states, where the two excited electrons populate shells of different principle quantum number, $n << n'$. These states may be the result of double capture into shells of comparable principle quantum numbers ($n \approx n'$) followed by an Auger transition, as suggested by Roncin et al. [65]. Hansen and collaborators [66] and Karim et al. [67] have recently calculated radiative and Auger decay rates for selected configurations of multiply excited ions. The ab–initio calculations of Vaeck

and Hansen [66] predict that for increasing asymmetry of a doubly excited state auto–ionization becomes less important and radiative transitions possible, in agreement with reference [5]. Close–coupling calculations of Chen and Lin [68] suggest a noticeable amount of radiative transitions (i.e. relatively large fluorescence yields) in certain quasi symmetric configurations of high lying doubly excited Ar^{16+} states.

Multiply excited projectiles such as generated in the case of incident Bi^{46+} ions (Fig. 3b) offer a large number of auto–ionizing transitions between the very many excited states of the hollow ion. These transitions can be combined to an even larger number of possible relaxation cascades such that a rigorous theoretical treatment of the relaxation process is currently out of reach. A simple relaxation scheme [51] that is based on intuition, basic features of emitted electron spectra, and wave function overlap arguments has led to realistic final charge states of the relaxed projectile. So far, this scheme does not resolve angular momentum states within a shell of principle quantum number n. However it may be extended and fine tuned to observed emitted electron and X-ray spectra. It consists in prioritizing possible relaxation steps and does not rely on detailed transition rates. For any configuration of the relaxing ion, the most likely next (Auger or radiative) transition is assumed to happen instantaneously and with unit probability. This relaxation model can be summarized as follows:

- Since Auger transitions are driven by electron–electron correlation in the initial state, the relaxation cascade is assumed to start with transitions that i) involve electrons in the outermost occupied shell(s) of the hollow ion and ii) minimize the kinetic energy of the emitted electrons. This agrees with the general observation of very strongly enhanced emitted electron energy spectra close to the continuum threshold, as well as with a relatively large wave function overlap between initial and final state. Our relaxation scheme gives highest priority to active electron pairs in identical or adjacent outer shells. Among these pairs, those are favored that include the most highly excited outer electron. Next on the priority list are transitions with the smallest possible change in principal quantum number of the inner electron that still lead to emission. This pattern is repeated until the ion is stable with respect to Auger decay.
- Radiative transitions may continue to relax the excited ion. Since radiative transition probabilities are largest for the lowest lying final states and, among those, for the lowest emitted photon energies [69], we first allow for transitions into the lowest vacancy and repeat this scheme until all inner vacancies are filled.

Figure 6 shows results for incident 830 keV Bi^{46+} ions, including the downstream relaxation of the projectile. As a consequence of the downstream relaxation process, most of the captured electrons get auto–ionized, as is easily seen by comparing the projectile charge states in Figure 6a with Figure 5b. The incident projectile charge effectively changes by no more than a few units. As suggested by a simple order–of–magnitude comparison of the collision time and typical Auger transition times (cf. Table I), auto–ionization is practically restricted to downstream deexcitations that happen after the collision. The simulated yields of emitted Auger electrons and X-rays in Figures 6b and 6c are accumulated over 234 eV wide intervals of emitted electron and photon energies, respectively. They are normalized to the area perpendicular to the incident beam direction that intersects projectiles with impact parameters between $b_{min} = 17$ and $R_1^* = 57.0$. For collisions in this impact parameter range the total X-ray yield divided by total Auger yield amounts to 0.03.

VI. PROJECTILE KINETIC ENERGY GAIN

The amount of potential energy of the collision system that is transferred into kinetic energy due to charge exchange processes can be obtained by integrating the net force between target and projectile along the trajectory. In the center–of–mass frame of reference, this amounts to integrating the force that governs the motion of the projectile of reduced mass along its trajectory. It defines the *'nuclear' energy defect* Q_{nuc} [52], which is directly related to the motion of the reduced–mass projectile considered as a structure-less particle of variable charge. The net force is the sum of the direct Coulomb and image charge interactions between target and projectile and is provided as a function of time within the dynamical COM.

Due to energy conservation, Q_{nuc} is identical to the difference of the total electronic binding energy of the collision system before and after the collision. This *'electronic' energy defect* is denoted by Q_{el} [52]. Since any COM–based simulation includes approximations to the complex dynamics of the multi–particle collision system that affect the coupling between nuclear and electronic degrees of freedom, the calculated values for Q_{el} and Q_{nuc} are expected to differ. Thus, the difference $|Q_{nuc} - Q_{el}|$ is indicative for the reliability of simulated translational kinetic energy gains. The electronic and nuclear energy defects for incident 46.2 keV Ar^{14+} ions are compared in Figure 7. The structure in Q_{el} is due to binning effects (i.e., it is related to the assignment of classical energy intervals to discrete quantum levels within the COM), and the two defects agree within the overall accuracy of the COM.

In order to compare theory with measured projectile energy–gain spectra, the critical radii for the sequential capture of electrons may be related to energy defect values and to the number of electrons that are captured for a particular impact parameter. For impact parameters $b_i = R^*_{i+1}$, i electrons have been captured, and the corresponding energy defects are $Q_{nuc}(b_i)$ and $Q_{el}(b_i)$. The simulated, discrete energy defects are folded with a Gaussian distribution R in order to correct for the finite experimental energy resolution. The full width at half maximum of R is adjusted to the resolution of the experiment. The simulated energy gain spectrum is now given by the cross section

$$\frac{d\sigma}{d\Delta E} = \sum_i \sigma_i \, R(\Delta E - Q_i) \tag{5}$$

which is differential in the projectile kinetic energy gain ΔE.

This method allows for the interpretation of peaks in measured spectra in terms of the corresponding numbers of captured electrons. In conjunction with the simulated projectile occupation changes, it also allows for the assignment of final projectile shells into which capture occurs at particular energy gains. Figure 8 shows a measured differential energy gain spectrum from Selberg *et al.* [39] together with the simulated spectrum for the removal of a specific number of electrons from C_{60} [52]. Experimental and calculated spectra are absolute, both in intensity (peak heights) and energy gain. Calculated energy gains correspond to the nuclear defects and include the five lowest energy gains. In the overall trend, the lower part of the measured spectrum, which yields the dominant contribution to the total cross section, agrees well with the simulation. The calculated nuclear energy defects are indicated by numbered arrows and correspond to capture into specific projectile shells (1: capture into $n = 12$, 2: into $n = 11$, 3: into $n = 11$, 4: into $n = 10$, 5: into $n = 10$). The high energy gain region cannot be explained by the present dynamical COM, and further investigations are necessary to understand this part of the kinetic energy gain spectra. Similarly, even

though reproducing the main features of the low–energy part of measured energy gain spectra on an absolute scale, the COM needs further refinement in order to more accurately agree with measured gains, e.g., for the capture of two electrons in Figure 8. A rewarding step in this direction could be the inclusion of projectile sub-shells nl which are not resolved within the current version of the COM.

VII. PROJECTILE ANGULAR DISTRIBUTIONS

Simulations for slow highly charged ions colliding with C_{60} have predicted [49,50] that the deflection function, i.e. the projectile scattering angle as a function of impact parameter, is characterized in its overall trend by two broad maxima that originate in the competition between attractive induced polarization and repulsive Coulomb interactions between the (charged) target and projectile. These maxima lead to strong enhancements in the angle–differential scattering cross section, usually referred to as 'Rainbow–Scattering'.

Recently, Walch *et al.* [35] have measured the angular distributions of 2.5 keV Ar^{8+} projectiles following the capture of 1 to 5 electrons from C_{60}. An experimental angle resolution of ≈ 0.01 degrees pointed to a potentially measurable prominent structure in the angle–differential cross section. In the experiment, the number of captured electrons was determined by measuring in coincidence the scattered projectile and a charge-state-analyzed intact C_{60} recoil ion. The observed angular distributions in Figure 9 show a strong increase of the deflection angle with the number of electrons removed from C_{60}, due to the increasing Coulomb repulsion between positively charged collision partners.

Comparison with calculations based on the dynamical COM [35] shows good agreement only if the influence on the projectile trajectory by the large polarizibility of the C_{60}^{i+} target is taken into account. This means that due to the large polarizability of C_{60}, the trajectory of a highly charged ion capturing electrons in the 'soft' over-barrier region of impact parameters is affected measurably by the induced target polarization. This effect is a truncated analog of the image charge acceleration for highly charged ions incident on solid surfaces [28]. It offers the interesting prospect of making the collective dielectric response of the cluster target observable in scattering experiments.

Calculated angular distributions, including the attractive self–image interaction of the projectile with the dipole it induces in the target, are shown in Figure 9 as solid lines. The same simulations without the induced polarization effects are shown as dotted lines. The agreement between the COM simulation and experiment in the location of the maxima is remarkable, showing that the model describes the basic interaction very well, even to the detail of the angular distributions. The effect of the induced target polarization on the deflection of the projectile is clearly observed in all cases shown.

With deflection functions provided by the COM, it should be possible to experimentally control the impact parameter. This provides the experimentalist with a new parameter for the study of the extraction of electrons from solid-like targets as a function of the distance of closest approach to the (curved) surface. It also allows for the investigation of questions such as how close the projectile can pass without disintegrating the C_{60} cage, which is closely related to the question of how much total energy is transferred to the C_{60} internal degrees of freedom as a function of impact parameter.

Furthermore, the pronounced influence of the target polarizability on the projectile deflection points to future refined investigations of the dielectric response of many-electron targets by measuring scattering distributions in recoil coincidence experiments.

VIII. REMARKS ON CHARGE LOCALIZATION AND MOBILITY ON C_{60}

The careful study of localization and mobility of capture–induced positive charge on C_{60} [56] is of interest to the new field of fullerene chemistry in possibly helping to better understand the formation of chemical bonds with fullerenes [70]. Furthermore, it may point to dominant fragmentation mechanisms of charged fullerenes [54].

Bárány and Setterlind [16] included a multipole expansion of the net electronic potential in their model. Applications of their model to electron transfer between multiply-charged ions and C_{60} and between C_{60} targets and charged C_{60} projectiles suggested that the charge left on the target cluster by electron removal may not be uniformly distributed on the cage surface, but localized near the surface [56]. Energy-gain measurements by Selberg et al. [39] showed distinct peaks in the energy-gain spectrum which could be attributed to discrete numbers of electrons removed from the target. Selberg et al. used a combination of energy-gain and cross section measurements to deduce that the charge removed from C_{60} is, at least initially, localized near the point of emission. They also concluded that this charge redistributes quickly following the initial electron transfer, on a time scale that is short compared to the overall collision time.

In contrast, in the dynamical COM [48–52], within which the results of the previous sections in this chapter were calculated, C_{60} is taken to be a conducting sphere. For distant collisions the fully delocalized net positive charge on C_{60} can then be thought of as localized at the center of the cluster. Deflection functions calculated under this assumption are shown in Figure 9 and, as a function of the impact parameter, in Figure 10a. In order to investigate the possible effect of a non-equilibrium charge distribution on the projectile deflection angle, simulations were carried out within the COM of Section II in which the target charge q_t was displaced from the center by a distance r_0 equal to the cage radius a=6.7 a.u. toward the projectile, on an axis joining the target center-of-mass and the projectile. Obviously, this simulation represents an extreme case for which the positive charge transferred to the C_{60} cage is not allowed to relax at all following transfer. The corresponding scattering angles in Figure 10b are much too large to be consistent with the measured data.

A more realistic treatment would allow the transferred charge to relax to the conducting sphere distribution over some characteristic time τ. Estimating the average collision time of conduction electrons as $\tau = \sigma m/Ne^2$ [71] where σ is the conductivity of graphite ($7 \times 10^4\ \Omega^{-1}\ m^{-1}$ [72]), m the electron mass, N the free electron density (taken to be of order of $10^{29}\ m^{-3}$) and e the electronic charge leads to a value of $\tau \sim 10^{-17}$ sec. Interestingly, a similar estimate for τ is obtained by considering the neutralization time of a positive charge on the surface of a classical electron gas of the same conductivity σ [27]. This estimate leads to $\tau = 1/(2\pi\sigma) \approx 10^{-16}$ s, which is much shorter than the collision time of 10^{-14} s. Such a short time would result in nearly instantaneous charge distribution relaxation with no effect on the projectile scattering due to charge localization at the emission site. The agreement between theory and experiment seen in Figure 9, and the unrealistically large scattering angles in Figure 10b, suggest that τ is indeed much shorter than the collision time.

Cameron and Parks [73] have measured charge–exchange rates for Paul–trapped $C_{60}^{i+}, i = 1...3$ ions in collisions with alkali atoms. Their model calculation reproduced the experimental data by assuming a symmetric distribution of capture–induced point charges on the surface of C_{60}. These localized positive surface charges were furthermore allowed to be mobile, such that the distribution of point charges is able to adjust (as a rigid rotator) to the moving projectile during the collision and to quickly redistribute to a new symmetric distribution after the exchange of an electron. The authors suggest that the seemingly contradictory properties of localization and mobility may be compatible due to the Jahn–Teller effect. In this case the break down of the Born–Oppenheimer approximation would induce distortions of the carbon cage and support mobile, but localized, surface charges.

IX. SUMMARY

The dynamical COM simulates the formation of hollow ions during the interaction of slow, highly charged ions with C_{60}. This chapter has put together several applications of the dynamical COM to observables that have recently been measured in this new type of heavy–ion collisions. Furthermore, it has analyzed the downstream relaxation of collisionally produced hollow ions within a simple relaxation scheme which allows for the simulation of energy differential and total yields of post–collisionally emitted projectile Auger electrons and photons.

The close agreement between the dynamical COM and various measured quantities confirm the picture of large-impact-parameter capture from C_{60} as an over-barrier process, very similar to corresponding processes in both ion-atom and ion-surface collisions. Future investigations, both experimental and theoretical, are necessary to refine these simulations in order to better understand the exciting life of a hollow ion during and after its interaction with a many–electron target, such as C_{60}.

Acknowledgments

This work was supported by the Division of Chemical Sciences, Office of Basic Energy Sciences, Office of Energy Research, U.S. Department of Energy and by the Kansas Center for Advanced Scientific Computing sponsored by the NSF/K*STAR program. Stimulating discussions and the collaboration with A. Bárány, H. Cederquist, C.L. Cocke, B. Fricke, L. Hägg, C.J. Setterlind, and B. Walch are gratefully acknowledged.

Bibliography

[1] E.K. Janev and L.P. Presnyakov, Phys. Reports **70**, 1 (1981); E.K. Janev and H. Winter, Phys. Reports **117**, 265 (1985).

[2] M. Barat and P. Roncin, J. Phys. B**25**, 2205 (1992).

[3] C.L. Cocke in "Review of Fundamental Processes and Applications of Atoms and Ions," ed. C.D. Lin, p. 111 (World Scientific, Singapore, 1993).
[4] P. Benoit–Cattin, A. Bordenave–Montesquieu, M. Boudjema, A. Gleizes, S. Dousson, and D. Hitz, J. Phys. B **21**, 3387, (1988).
[5] R. Ali, C.L. Cocke, M.L.A. Raphaelian, and M. Stöckli, J. Phys. B **26**, L117, (1993); Phys. Rev. A **49**, 3586 (1994).
[6] M. Schulz, C.L. Cocke, S. Hagmann, and M. Stöckli, Phys. Rev. A **44**, 1653 (1991).
[7] S. Winecki, C.L. Cocke, D. Fry, and M.P. Stöckli, Phys. Rev. A **53**, 4228 (1996).
[8] J. Burgdörfer, P. Lerner, and F.W. Meyer, Phys. Rev. A **44**, 5674 (1991).
[9] J. Burgdörfer, in *Review of Fundamental Processes and Applications of Atoms and Ions*, ed. C. D. Lin, p. 517, (World Scientific, Singapore, 1993).
[10] J. Burgdörfer, C. Reinhold, and F.W. Meyer, Nucl.Instrum.Methods Phys. Res. B **98**, 415 (1995).
[11] M.W. Clark, D. Schneider, D. Dewitt, J.W. McDonald, R. Bruch, U.I. Safranova, I.Y. Tolstikhina, and R. Schuch, Phys. Rev. A **47**, 3983 (1993).
[12] J.P. Briand, B. d'Etat-Ban, D. Schneider, M.A. Briere, V. Decaux, J.W. McDonald, and S. Bardin, Phys. Rev. A**53**, 2194 (1996).
[13] F.W. Meyer, C.C. Havener, and P.A. Zeijlmans van Emmichoven, Phys. Rev. A **48**, 4476 (1993).
[14] Q. Yan, D.M. Zehner, and F.W. Meyer, Phys. Rev. A **54**, 641 (1996).
[15] H. Kurz, F. Aumayr, HP. Winter, D. Schneider, M.A. Briere, and J.W. McDonald, Phys. Rev. A **49**, 4693 (1994).
[16] A. Bárány and C.J. Setterlind, Nucl.Instrum.Methods Phys. Res. B.**98**, 407 (1995).
[17] A.G. Borisov, R. Zimny, D. Teillet–Billy, and J.P. Gauyacq, Phys. Rev. A **53**, 2457 (1996).
[18] J. Limburg, S. Schippers, I. Hughes, R. Hoekstra, R. Morgenstern, S. Hustedt, N. Hatke, and W. Heiland, Phys. Rev. A. **51**, 3873 (1995).
[19] W. Huang, H. Lebius, R. Schuch, M. Grether, and N. Stolterfoht, Phys. Rev. A**56**, 3777 (1997).
[20] J. Thomaschewski, J. Bleck-Neuhaus, M. Grether, A. Spieler, and N. Stolterfoht, Phys. Rev. A**57**, 3665 (1998).
[21] P. Kürpick and U. Thumm, Phys. Rev. A**58**, 2174 (1998).
[22] C. Auth, and H. Winter, Phys. Lett. A **217**, 119 (1996).
[23] J. Limburg, S. Schippers, R. Hoekstra, R. Morgenstern, H. Kurz, F. Aumayr, and HP. Winter, Phys. Rev. Lett. **75**, 217 (1995).
[24] F. Aumayr, in Proceedings of the XIX'th Int. Conf. on the Physics of Electronic and Atomic Collisions, ed. L. Dubé et al., AIP Conf. Proc. 360, p. 631 (AIP press, New York 1995).
[25] L. Hägg, C.O. Reinhold, and J. Burgdörfer, Phys. Rev. A**55**, 2097 (1997); Nucl.Instrum.Methods Phys. Res. B **125**, 133 (1997).
[26] J.P. Briand, S. Thuriez, G. Giardino, G. Borsoni, V. Le Roux, M. Froment, m. Eddrief, C. de Villeneuve, B. d'Etat-Ban, and C. Sébenne, Phys. Rev. A **55**, R2523 (1997).
[27] J.J. Ducrée, F. Casali, and U. Thumm, Phys. Rev. A**57**, 338 (1998).
[28] H. Winter, Europhys. Lett. **18** 207 (1992); J. Phys.: Condens. Matter **8**, 10149 (1996).
[29] J.J. Ducrée, J. Mrogenda, E. Reckels, M. Rüther, A. Heinen, Ch. Vitt, M. Venier, J. Leuker, H.J. Andrä, and R. Díez Muiño, Phys. Rev. A**57**, 1925 (1998).
[30] H. Ryufuku, K. Sasaki and T. Watanabe, Phys. Rev. A**21**, 745 (1980).
[31] A. Niehaus, J. Phys. B**19**, 2925 (1986).
[32] A. Bárány, in Proceedings of the XVI Int. Conf. on the Physics of Electronic and Atomic Collisions, ed. Dalgarno et al, AIP Conf. Proc. 205, p. 246 (AIP, New York, 1990).
[33] P. Hvelplund, L.H. Anderson, H.K. Haugen, J.Lindhard, D.C. Lorents, R. Malhotra, and R. Ruoff, Phys. Rev. Lett. **69**, 1915 (1992).
[34] B. Walch , C.L. Cocke, R. Voelpel, and E. Salzborn, Phys. Rev. Lett. **72**, 1439 (1994).
[35] B. Walch, U. Thumm, M. Stöckli, C.L. Cocke, and S. Klawikowski, Phys. Rev. A **58**, 1261 (1998).
[36] T. LeBrun, H.G. Berry, S.Cheng, R.W. Dunford, H.Esbensen, D.S. Gemmel, and E.P. Kanter, Phys. Rev. Lett. **72**, 3965 (1994).
[37] J.P. Briand, L. de Billy, J. Jin, H. Khemliche, M.H. Prior, Z. Xie, M. Nectoux, and D. Schneider, Phys. Rev. A **53**, R2925 (1996).
[38] J. Jin, H. Khemliche, M.H. Prior, Z. Xie, Phys. Rev. A **53**, 615 (1996).
[39] N. Selberg, A. Bárány, C. Biedermann, C.J. Setterlind, H. Cederquist, A. Langereis, M.O. Larsson, A.

Wännström, and P. Hvelplund, Phys. Rev. A **53**, 874 (1996).
[40] V.V. Afrosimov, A.A. Basalaev, V.P. Belik, Yu. V. Naide, M.N. Panov, and O.V. Smirnov, in "XX Conference on the Physics of Electronic and Atomic Collisions," ed. F. Aumayr, G. Betz and H.P. Winter, contributed abstracts, p. FR070 (unpublished, 1997).
[41] C.J. Setterlind, P. Sakurai, and A. Bárány, ibid., p. FR 073.
[42] T. Schlathölter, R. Hoekstra, and R. Morgenstern, ibid., p. FR077.
[43] J. Opitz, M. Benndorf, U. Wemer, U. Brinkmann, and B.A. Huber, ibid., p. FR 078, 079.
[44] J. Bernard, L. Chen, A. Denis, J. Désesquelles and S. Martin, Physica Scripta **T73**, 291 (1997).
[45] S. Martin, J. Bernard, L. Chen, A. Denis, and J. Désesquelles, European Phys. Journal D **4**, (1998).
[46] A. Itoh, H. Tsuchida, K. Miyabe, M. Imai and N. Imanishi, Physica Scripta **T73**, 289 (1997).
[47] A. Bárány, in "Photonic, Electronic, and Atomic Collisions" ed. F. Aumayr, G. Betz and H.P. Winter, p. 641 (World Scientific, Singapore 1998).
[48] U. Thumm, J. Phys. B **27**, 3515 (1994). In this reference, a factor 1/2 is not printed in the self-image protentials. This factor, however, was included in all computations. In addition, the present work uses a different sign convention in the definition of interaction potentials.
[49] U. Thumm, J. Phys. B **28**, 91, (1995).
[50] U. Thumm, T. Baştuğ, and B. Fricke, Phys. Rev. A **52**, 2955 (1995).
[51] U. Thumm, Phys. Rev. A **55**, 479 (1997).
[52] U. Thumm, A. Bárány, H. Cederquist, L. Hägg, and C.J. Setterlind, Phys. Rev. A **56**, 4799 (1997).
[53] D.C. Lorentz, Comments At. Mol. Phys. **33**, 125 (1997).
[54] P. Scheier, B. Dünser, R. Wörgötter, S. Matt, D. Muigg, G. Senn, and T.D. Märk, Int. Rev. in Phys. Chem. **15**, 93 (1996).
[55] D. Hathiramani, V. Schäfer, K. Aichele, U. Hartenfeller, F. Scheuermann, M. Steidl, M. Westermann, and E. Salzborn, in "Photonic, Electronic, and Atomic Collisions" ed. F. Aumayr, G. Betz and H.P. Winter, p. 653 (World Scientific, Singapore 1998).
[56] H. Shen, P. Hvelplund, D. Mathur, A. Bárány, H. Cederquist, N. Selberg, and D.C. Lorentz, Phys. Rev. A **52**, 3847 (1995).
[57] H.G. Busmann, Th. Lill, B. Reif, and I.V. Hertel, Surf. Sci. **272**, 146 (1992).
[58] M.J. Puska and R.M. Nieminen, Phys. Rev. A**47**, 1181 (1993).
[59] J.L Martins, N. Troullier, and J.H. Weaver, Chem. Phys. Lett. **180**, 457 (1991).
[60] C. Yannouleas, and U. Landman, Chem. Phys. Lett. **217**, 175 (1994).
[61] T. Baştuğ, P. Kürpick, J. Meyer, W.–D. Sepp, B. Fricke, and A. Rosen, Phys. Rev. B **55**, 5015 (1997).
[62] C. Lifshitz, M. Iraqi, T. Peres, and J.E. Fischer, Rapid Commun. Mass Spectrom. **5**, 238 (1991).
[63] I.V. Hertel, H. Steger, J. de Vries, B. Weisser, C. Menzel, B. Kamke, and W. Kamke, Phys. Rev. Lett. **68**, 784 (1992).
[64] P. Sakurai, M.Sc. Thesis, Univ. Stockholm, unpublished (1997).
[65] P. Roncin, M.N. Gaboriaud, and M. Barat, Europhys. Lett. **16**, 551, (1991).
[66] N. Vaeck and J.E. Hansen, J. Phys. B **28**, 3523, (1995), and ref.s therein.
[67] K.R. Karim, S.R. Grabbe, and C.P. Bhalla, J. Phys. B **29**, 4007 (1996).
[68] Z. Chen and C.D. Lin, J. Phys. B **26**, 957, (1993).
[69] E.U. Condon, G.H.Shortley, *The Theory of Atomic Spectra*, (Cambridge University Press, 1957), pp. 136, 148.
[70] S. Petrie, J.Wang, and D.K. Bohme, Chem. Phys. Letters **204**, 473 (1993).
[71] C. Kittel, "Introduction to Solid State Physics," p. 142 (Wiley, New York, 1986).
[72] Handbook of Chemistry and Physics, ed. R.C. Weast, p. F-140 (Chemical Rubber Co., Cleveland, 1962).
[73] D.B. Cameron and J.H. Parks, Chem. Phys. Lett. **272**, 18 (1997).

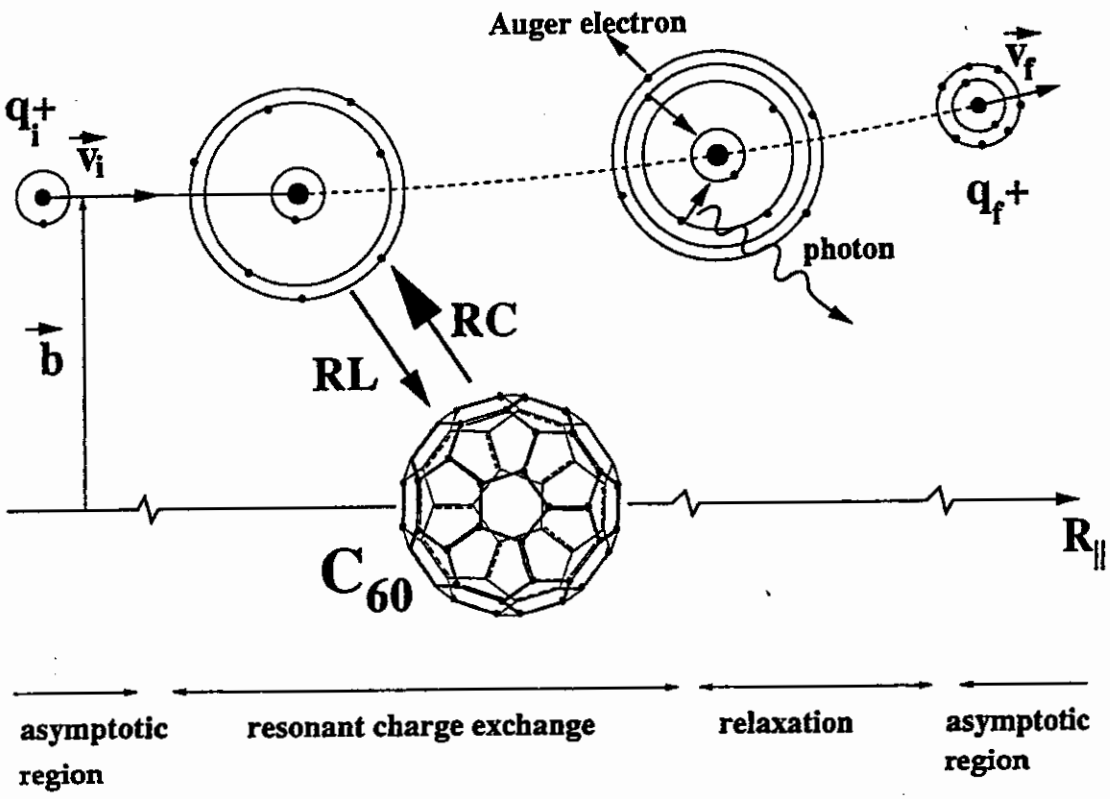

Figure 1. Sketch of the collisions scenario (not to scale). A highly charged ion with initial charge q_i, velocity $\vec{v}_i$, and impact parameter $\vec{b}$ carries one tightly bound electron into the collision. At distances of the order of 10 to 100 a.u. from the target center it resonantly captures (RC) and (to a lesser extent) loses (RL) electrons. This leads to a positively charged target and a multiply excited, hollow projectile. Downstream and past the resonant interaction region, the unstable hollow projectile relaxes by emitting Auger electrons and X-ray photons. It may then be detected with final charge state q_f and velocity $\vec{v}_f$. The projection of the target--projectile distance R onto the incident--beam direction is denoted by $R_{||}$.

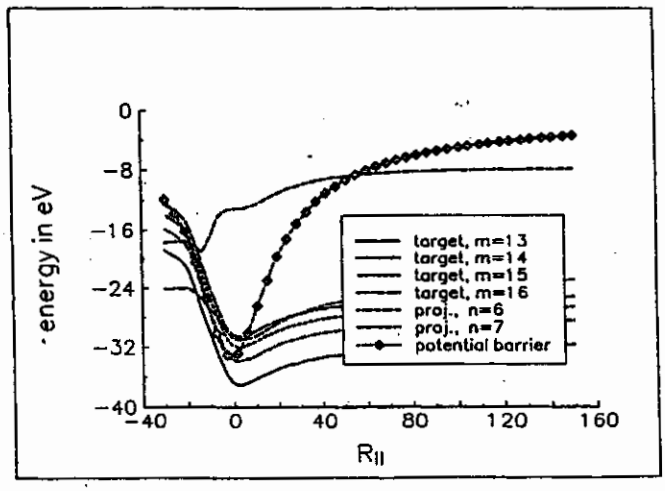

Figure 2. Shift of target and projectile energy levels relative to the potential barrier for classical over--barrier capture as a function of the distance $R_{||}$ for 80 keV Ar^{8+} ions colliding with C_{60} at impact parameter b = 15 (see text).

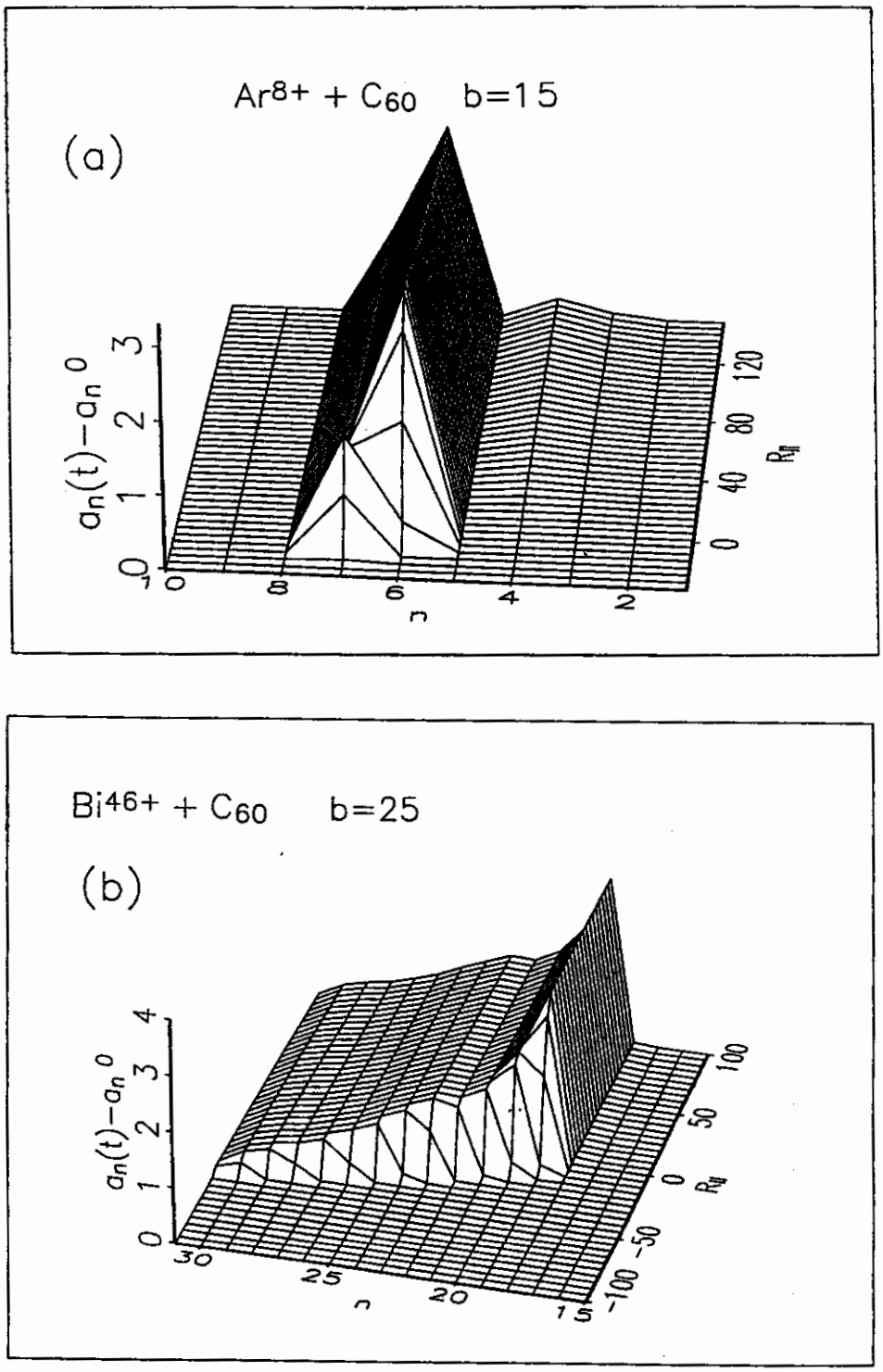

Figure 3. Evolution of projectile level occupations in collisions with C_{60}. The point of closest approach is at $R_{\|} = 0$. (a) For incident 80 keV Ar 8+ projectiles and impact parameter b = 15 [48]. The graph shows the dynamical change $a_n(t) - a_n^0$ in population of projectile shells $n = 1$ to $n = 10$. The initial shell population is denoted as a_n^0. $a_n(t)$ is the population at the distance $R_{\|}(t)$. (b) For 830 keV Bi^{46+} and $b = 25$ [51].

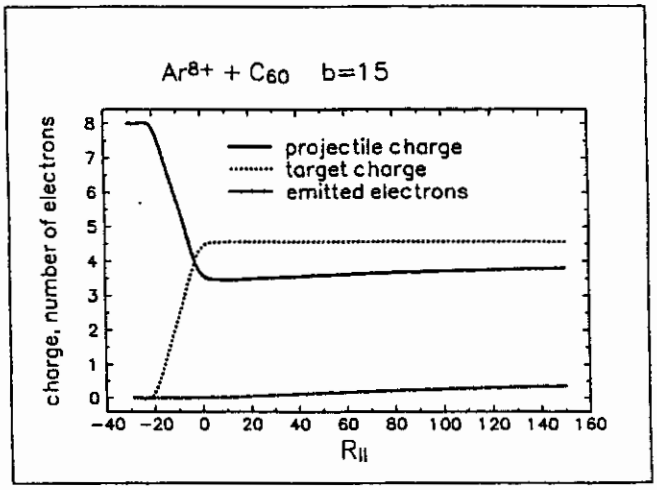

Figure 4. Projectile and target charge–state evolution and projectile Auger emission for incident 80 keV Ar^{8+} projectiles colliding with C_{60} at impact parameter $b = 15$ [48].

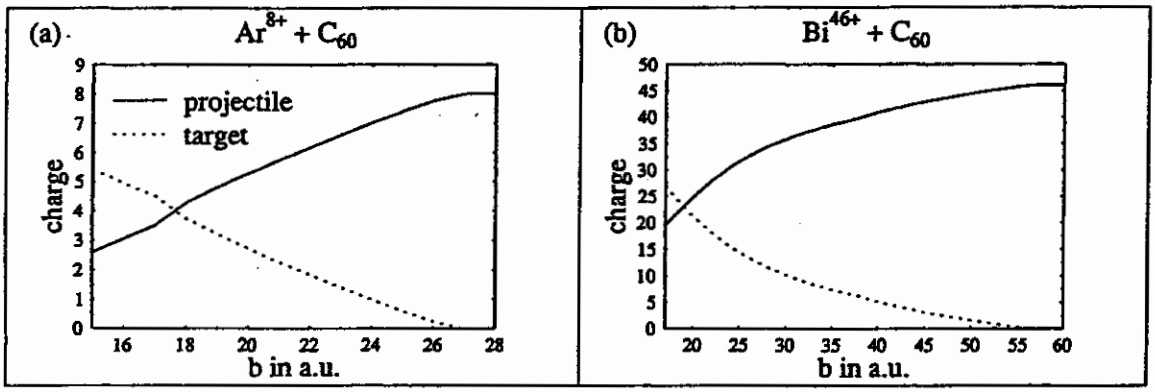

Figure 5. Projectile and target charge states as a function of the impact parameter b immediately after resonant electron exchange has ceased at $R_{\|} = 150$. (a) for incident 26.4 keV Ar^{8+} projectiles [52]. (b) for 830 keV Bi^{46+} [51].

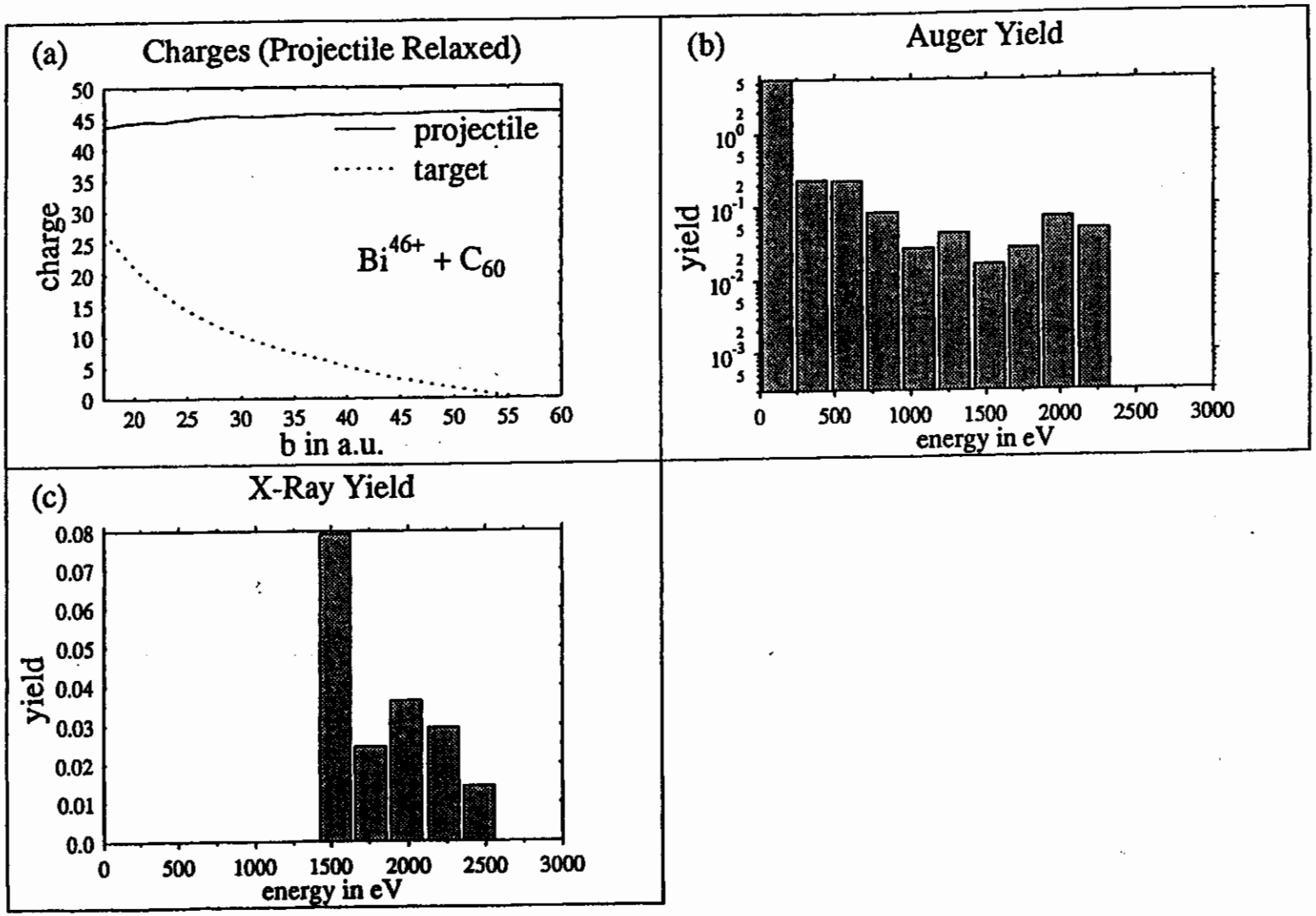

Figure 6. Results for 830 keV Bi $^{46+}$ colliding with C_{60} , including downstream projectile relaxation [51]. (a) Projectile and target charge states as a function of the impact parameter *b*. (b) Simulated Auger electron yield. (c) Simulated X-ray yield.

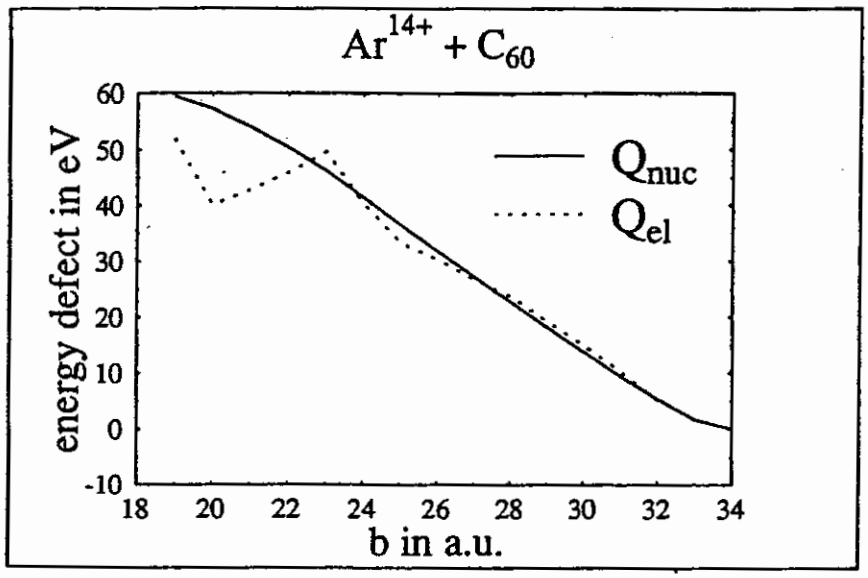

Figure 7. Electronic and nuclear energy defects as a function of the impact parameter b, converged at a distance of $R_{\parallel} = 50000$ a.u. downstream, for 46.2 keV Ar^{14+} colliding with C_{60}.

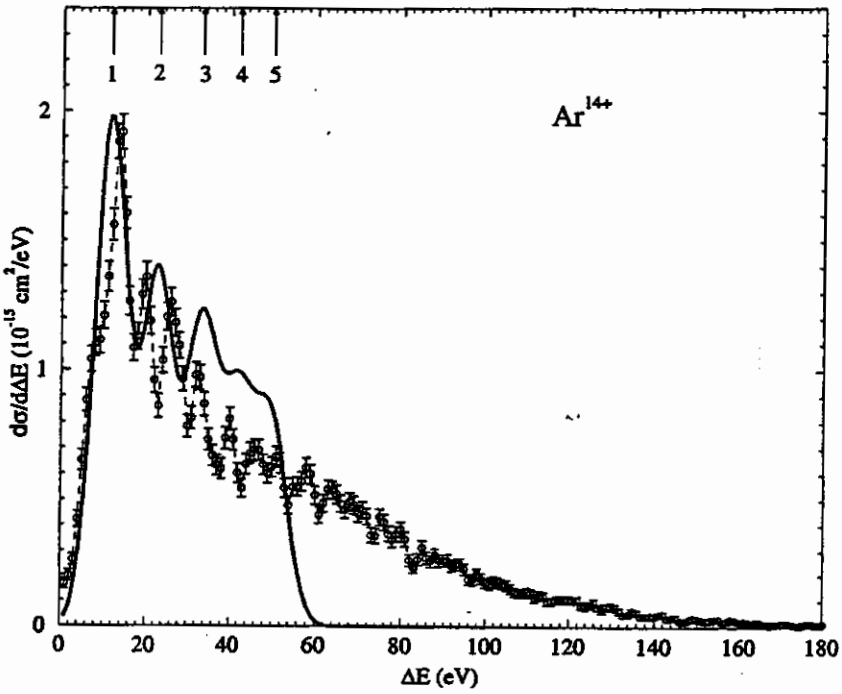

Figure 8. Simulated and measured projectile energy gain spectra for 46.2 keV Ar^{14+} - C_{60} collisions. The measured [39] and calculated [52] energy gain values and peak heights (cross sections) are absolute. The experimental errors in peak positions are typically ±0.5 eV. The arrows point to the calculated nuclear energy defects for the capture of 1, 2, 3. etc.. electrons.

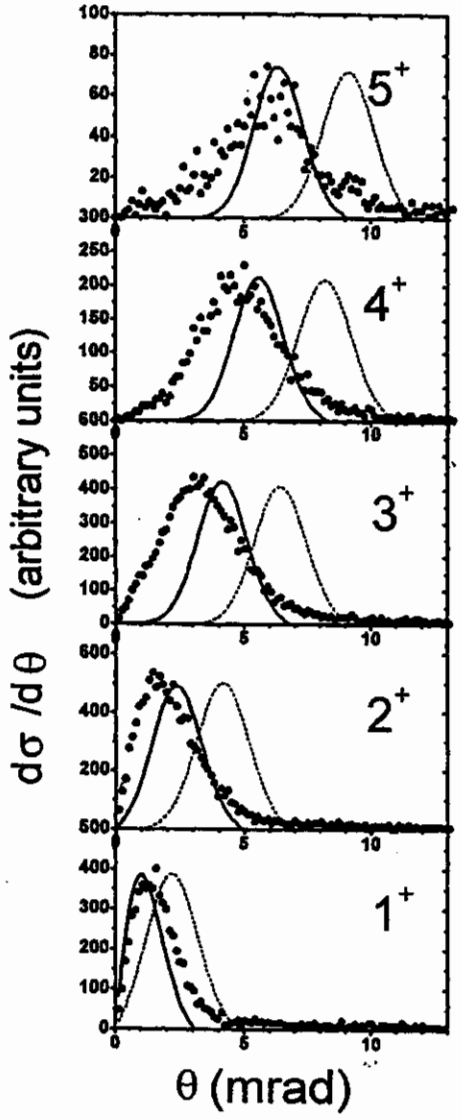

Figure 9. Angular distributions for the capture of i=1...5 electrons from C_{60} by 2.5 keV Ar^{8+} ions [35]. Each figure is labeled by i+. 'Theta' is the deflection angle. The solid curves are dynamical COM calculations including target polarization. The dotted curves are calculated without this polarization.

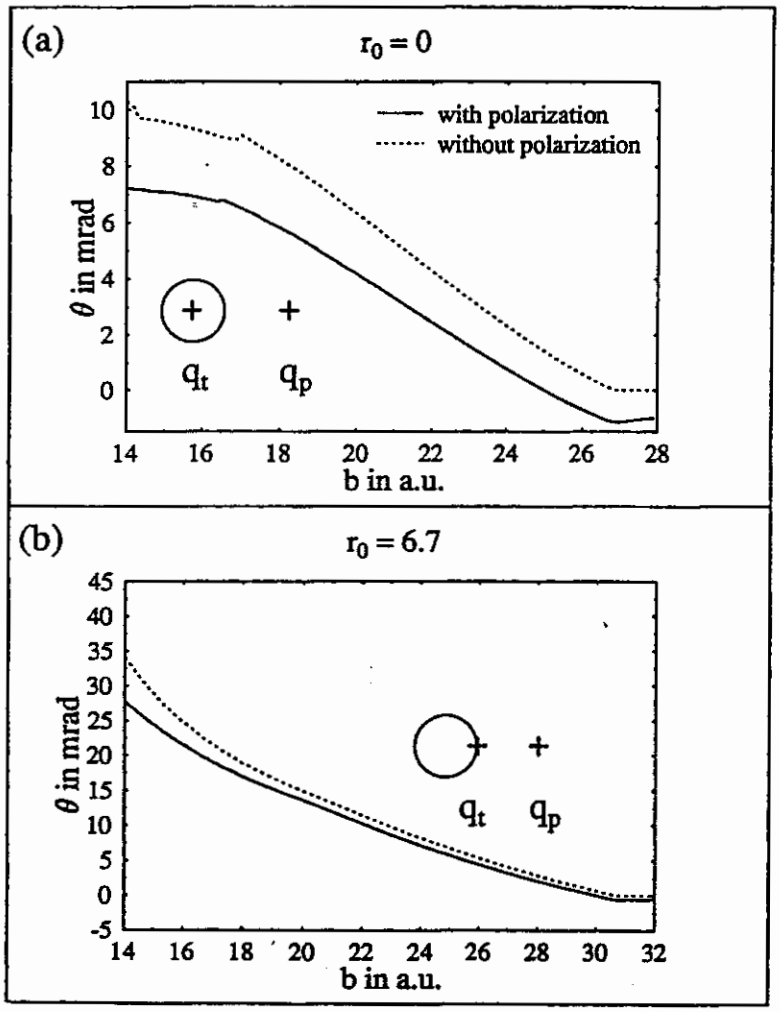

Figure 10. Simulated projectile deflection angles for 2.5 keV Ar^{8+} on C_{60} collisions. Results 'with' and 'without' polarization refer to the inclusion (omission) of induced polarization interactions (see text). (a) Simulations carried out by assuming instantaneous and uniform distribution of capture-generated positive charges on the C_{60}. (b) Deflection function calculated under the assumption that the net target charge remains localized on surface of C_{60}, facing the projectile.

Table I. Time scales relevant for the formation and relaxation of hollow ions (of core charge q_{core}). Typical values for 80 keV Ar^{8+} interacting with C_{60}. The plasmon response time is estimated by $\sqrt{\frac{2\pi}{n_{el}}}$, where n_{el} is the average electron density of C_{60}.

collision time for resonant exchange:	5 fs
orbiting time of first active projectile level (n=7):	0.8 fs
plasmon response time of C_{60}:	0.2 fs
average time between successive electron capture events:	0.3 fs
projectile Auger transitions:	> 0.1 fs
projectile radiative transitions:	$q_{core}^{-4} \cdot 10^{-8}$ s

Table II. Critical over–barrier radii R_i^* for the production of final target charge states $+i$ in collisions with C_{60} for various incident projectile ions: 50 keV N^{5+} [49], $3.3q$ keV Ar^{q+}, $q = 8, 15$ [52], and 830 keV Bi^{46+} [51].

i	N^{5+}	Ar^{8+}	Ar^{15+}	Bi^{46+}
1	22.1	26.9	34.8	57.0
2	16.0	23.9	31.4	52.0
3	13.6	21.6	28.9	48.7
4		19.4	26.7	45.3
5		17.7	24.8	42.7
6		15.9	23.0	40.2
7				38.2
8				36.0
9				33.8
10				31.9
11				30.3
12				29.0

Table III. Geometrical cross sections σ_i (in 10^{-15} cm^2) for the production of final target charge states $+i$ for 50 keV N^{5+} [49], $3.3q$ keV Ar^{q+}, $q = 8, 15$ [52], and 830 keV Bi^{46+} [51] colliding with C_{60}. σ_{tot} and σ_{tot}^{exp} are the calculated and measured [34,39] total cross sections for charge–state changing collisions. The projectile shell n into which capture primarily occurs are given in parenthesis.

	N^{5+}	Ar^{8+}	Ar^{15+}	Bi^{46+}
σ_1 (n)	20.4 (5)	13.4 (7)	19.8 (12)	47.8
σ_2 (n)	6.3 (4)	9.2 (7)	13.3 (12)	29.1
σ_3 (n)		7.9(7)	10.8 (11)	28.0
σ_4 (n)		5.6 (6)	8.6 (10)	20.1
σ_5 (n)		5.3 (6)	7.6 (10)	18.2
σ_6 (n)				13.8
σ_7 (n)				14.3
σ_8 (n)				13.5
σ_9 (n)				11.0
σ_{10} (n)				8.8
σ_{11} (n)				6.8
σ_{tot}	42.9	63.7	107	286
σ_{tot}^{exp} [39]		46±14	100±31	
σ_{tot}^{exp} [34]		44±18		